# Quantification of polyimide carbonization after laser ablation

F. Raimondi, S. Abolhassani, R. Brütsch, F. Geiger, T. Lippert,[a] J. Wambach, J. Wei, and A. Wokaun
*Paul Scherrer Institut, CH-5232 Villigen PSI, Switzerland*

(Received 16 May 2000; accepted for publication 26 June 2000)

Polyimide was irradiated with a XeCl excimer laser (308 nm) and the ablated area and its surrounding were studied using transmission electron microscopy (TEM) and confocal Raman microscopy. Ring-like structures surrounding the ablated area were detected at all fluences. At fluences lower than 250 mJ/cm$^{-2}$ the formation of conical structures was observed within the irradiated area. The width of the rings increases with fluence and only slightly with the number of pulses. The rings consist mainly of polycrystalline carbon with a relatively high bond angle disorder, with thickness decreasing radially from the crater edge. The thickness of the deposited carbon was determined from TEM analysis and calculated from the intensity ratios of Raman bands assigned to carbon and polyimide using a two layer model. Comparing the two results an estimate of the absorption coefficient of the deposited carbon could be obtained. On top of the cone structures carbon was detected with a higher degree of crystallinity and lower bond angle disorder as compared to the material deposited outside the crater. With energy dispersive x-ray analysis, calcium could be detected on top of the cones. Therefore, it can be assumed that the Ca impurities are causing the cone structures. The higher crystallinity of the carbon inside the irradiated area is probably due to a tempering-like process on top of the Ca compound which is heated upon laser irradiation or to a mixture of growth mechanisms similar to the ones suggested for the formation of carbon nanotubes on metal particles and carbon nanohorns without metal catalysis. © *2000 American Institute of Physics.* [S0021-8979(00)04919-7]

## I. INTRODUCTION

Since the commercialization of Kapton™ polyimide numerous applications have been found. Polyimides are important materials in microelectronics, where they are used as dielectric in multichip modules (MCM),[1] but also as negative type photoresist.[2] The via-holes through the polyimide in the MCMs are produced by laser ablation.[3,4] Polyimides can be structured by all common excimer laser wavelengths (193, 248, 308, and 351 nm).[5] It is generally agreed on that the mechanism of ablation is mainly photothermal, with additional photochemical features, especially with 193 nm irradiation.[6] Prominent features of Kapton ablation are the sharp ablation threshold and differences in the ablation rate near the threshold between two very sensitive methods, i.e., atomic force microscopy and quartz microbalance.[7] Ablation products have been studied by a variety of techniques, e.g., infrared spectroscopy,[8] gas chromatography,[9] and mass spectrometry[10] have been used to identify the principal gaseous products of Kapton ablation. The main products are: $CO_2$, CO, $H_2O$, and HCN as well as various light hydrocarbons (up to four carbon atoms). Laser induced fluorescence measurements indicate that diatomic fragments $C_2$ and CN are also formed at least transiently during ablation.[11] Larger molecules (e.g., $C_{60}$) up to visible carbon particles are also detected.[12] The soot is partly redeposited around the ablation crater and consists mainly of carbon. The ablated area of Kapton was also analyzed using analytical techniques with high lateral resolution. Within a certain fluence range carbonization was detected, but the carbonized material is different from the material deposited in the surrounding of the ablation crater.[13,14] The carbonization results in an increase of the conductivity of up to 12 orders of magnitude.[15] Another important feature of ablation is the creation of microstructures within a certain fluence range. These microstructures can have the appearance of periodic, ripple-like structures or cone-shaped features.[16] Several formation mechanisms for these surface structures have been proposed in the literature: the presence of particulate impurities,[17,18] differences in the etch rates of crystalline and amorphous domains,[19] Marangoni convection in a molten surface layer,[20] stress release,[21] surface scattered waves,[22] and various simultaneously acting mechanisms.[23]

In this study the carbonization inside the crater, especially on top of the microstructures and in the surrounding of the ablation craters was studied by transmission electron microscopy (TEM) and confocal Raman microscopy. It was shown in recent years that Raman microscopy is a flexible tool for the investigation of polymer interfaces and the determination of the degree of structural order in carbonaceous materials.[24–27] It is therefore an ideal technique to study the laser induced carbonization on polymer surfaces.

## II. EXPERIMENT

Polyimide (Kapton™, DuPont) films (~125 $\mu$m thick) were supplied by Goodfellow and used as received. A XeCl excimer laser (Lambda Physik, Compex 205; $\lambda = 308$ nm, $\tau = 20$ ns) was used as irradiation source for the ablation ex-

[a]Electronic mail: thomas.lippert@psi.ch

 

periments. A pinhole mask (diameter 4 mm) was demagnified with a lens (focal length = 100 mm) onto the polymer surface to create ablation craters of ~250 $\mu$m diameter. The pulse energy was measured by a joulemeter (Gentec 200) and the irradiated area was determined by an optical microscope and a profilometer (Dektak 8000). Polyimide was irradiated with 200–800 pulses, at fluences ranging from 40 to 320 mJ/cm$^2$. The ablation craters and the surrounding area were studied with a confocal Raman microscope (Labram, DILOR) equipped with a 100× magnification objective (laser spot size $\leq 1$ $\mu$m) and a thermoelectrically cooled charge coupled device (CCD) detector (1152×300 pixels). The Raman spectra were obtained in a backscattering geometry with the green line ($\lambda = 530.9$ nm) of a Kr-ion laser (Coherent Innova 302). The power at the sample was kept at 200 $\pm 10$ $\mu$W. This value was low enough to prevent carbonization of the polymer, as shown by the constant Raman spectrum during acquisition. Raman spectra were routinely acquired in the range from 600 to 1900 cm$^{-1}$ using a 1800 grooves/mm grating. To extend the observation range to the frequency of the second-order region of the carbon Raman spectrum, some spectra were recorded with a 600 grooves/mm grating. The lateral resolution of the Raman microscope was about 2 $\mu$m.

All spectra showed an intense fluorescence background and were base line corrected, by subtracting the 7th order polynomial that fitted best the 600–1100 and 1650–1750 cm$^{-1}$ data regions. Figure 1 shows the base line corrected micro-Raman spectrum of polyimide, together with a Fourier transform (FT)-Raman spectrum obtained with a BRUKER FRA106/S spectrometer using 1064 nm radiation. In spite of the high fluorescence background and a resulting low signal-to-noise ratio, all spectral features of polyimide are detected in the micro-Raman spectrum. FT-Raman spectroscopy is not suitable to study carbonaceous materials because they strongly absorb IR radiation, which causes the thermal decomposition of the carbon material. In addition, FT-Raman spectroscopy does not have the spatial resolution required for the study of structures in the micrometer range.

The morphology of the samples was evaluated by scanning electron microscopy (SEM) using a 20 keV electron beam (after covering the sample with a 15-nm-thick Pt layer). Information on the elemental composition of selected regions was obtained by energy dispersive x-ray analysis (EDX). The lateral resolution of this technique for our samples is in the order of 5–10 $\mu$m.

One sample was especially prepared for TEM analysis. A line structure was obtained by overlapping a row of ten craters created by 800 pulses with 80 mJ cm$^{-2}$. The line structure allowed the preparation of samples for TEM analysis, using an ultramicrotome. The shape of this structure ensured that a microtome cut perpendicular to the line represents a section of the ablated area and its surrounding. The irradiated side of the polymer film was covered by sputtering a 180-nm-thick gold layer, prior to embedding the film in epon (epoxy embedding kit, Fluka). The gold layer protects, at least partly, the deposited material from the epon, simplifies the identification of the irradiated polymer side during TEM analysis, and defines the interface between the deposited material and the epon. The ultramicrotomy was carried out on a LEICA ultramicrotome. The sections were cut to a thickness of 80–100 nm and collected on a Cu grid with a carbon membrane. The sections were observed by a JEOL 2010 TEM operating at 200 keV. The microscope is equipped with an Oxford Instrument ISIS energy dispersive x-ray spectrometer and a Gatan multiscan CCD camera.

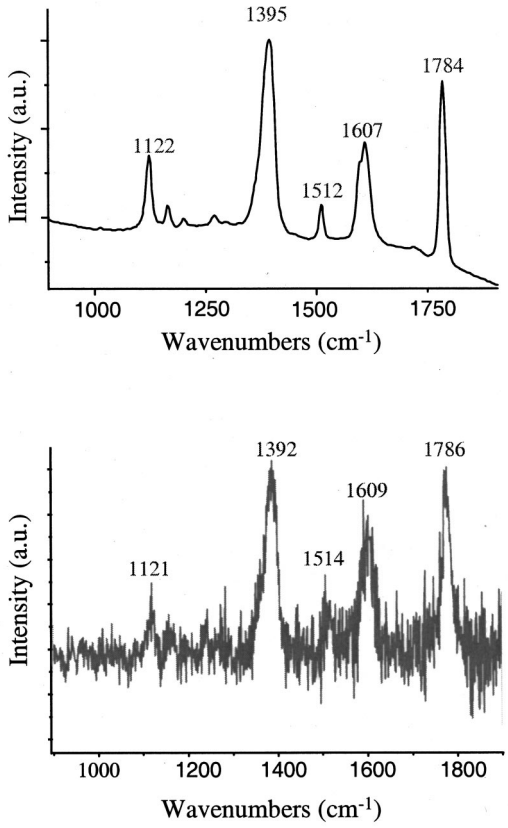


FIG. 1. Top: FT-Raman spectrum of polyimide with excitation wavelength 1064 nm. 1024 scans at a resolution of 4 cm$^{-1}$. Bottom: base line corrected micro-Raman spectrum of polyimide. Excitation wavelength 530.9 nm, power at the sample 200 $\mu$J, 100× magnification objective, and 1800 grooves/mm grating.

## III. RESULTS

### A. Morphological features

The 100× magnification optical picture of a typical ablation crater, obtained after irradiation with 200 pulses at 248 mJ/cm$^2$, is shown in Fig. 2(a). The crater, with sharp and well defined contours, has a diameter of ~250 $\mu$m and is surrounded by a black ring that extends ~200 $\mu$m from the edge of the crater. As reported previously and illustrated in Table I, the width of the ring evaluated with an optical microscope increases with the ablation fluence but is insensitive to the pulse number at a given fluence.[28]

A section of the TEM sample is shown in Fig. 3(a). The deposited material extends for $36 \pm 4$ $\mu$m (standard deviation from different samples) from the crater edge, in close agreement with the values determined by optical microscopy. The thickness of the deposited layer [shown in Fig. 3(b)] is $\sim 1.6 \pm 0.3$ $\mu$m near the edge of the crater and decreases nearly linearly with the distance from the crater. The rough

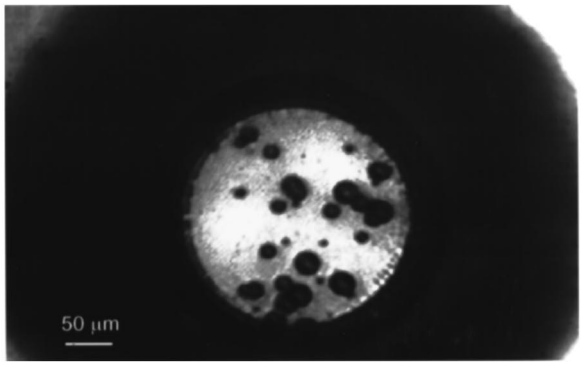


(a)

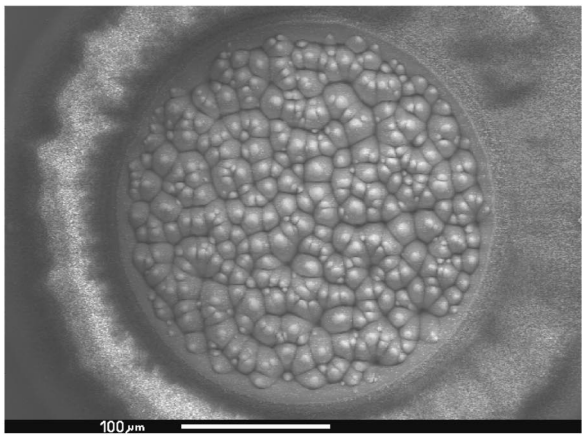


(b)

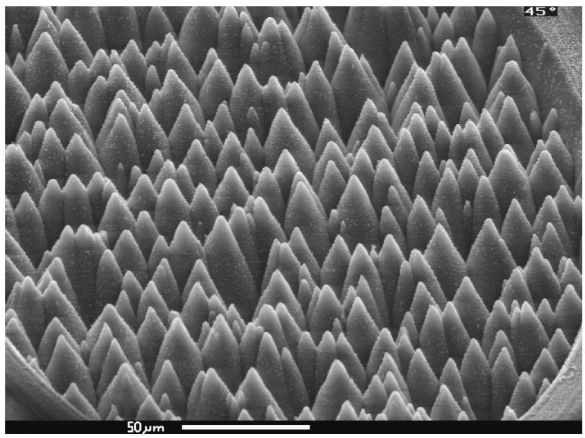


(c)

FIG. 2. (a) 100× magnification optical image of a crater ablated with 200 pulses at 248 mJ/cm$^2$. (b) and (c) SEM pictures of a crater ablated with 800 pulses at 160 mJ/cm$^2$.

surface and the inhomogeneous density of the deposited material are clearly visible (the lighter colors representing lower densities).

In Figs. 2(a)–2(c) the ablated area of the ''standard'' sample is shown. Below a laser fluence of 250 mJ/cm$^2$ the creation of cone-shaped structures is observed. In the video micrograph in Fig. 2(a) the cones are visible as dark spots, while their shape is clearly visible in the SEM pictures [Figs. 2(b)–2(c)]. The bottom of the ablation craters is flat after irradiation with fluences above 250 mJ/cm$^2$, while for irradiation with fluences below 160 mJ/cm$^2$ no flat bottom could be obtained. The number of conical structures increases with decreasing fluences. The height and diameter of the conical structures is not constant within a single ablation crater [Fig. 2(c)].

TABLE I. Dependency of the ring width on the fluence at constant number of pulses (right column) and on the number of pulses at constant fluence (left column). These values have been determined by optical microscopy using a 10× magnification objective, unless stated otherwise.

| 800 pulses | | 320 mJ/cm$^2$ | |
|---|---|---|---|
| Fluence (mJ/cm$^2$) | Ring width ($\mu$m) | Number of pulses | Ring width ($\mu$m) |
| 80[a] | 57 | 60 | 301 |
| 80 (TEM sample) | 41–54 | 140 | 306 |
| 116[a] | 78 | 250 | 303 |
| 158 | 93 | 400 | 312 |

[a]Value determined using a 50-fold magnification objective.

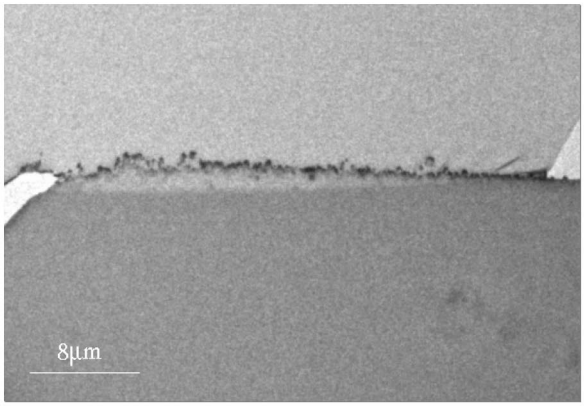


(a)

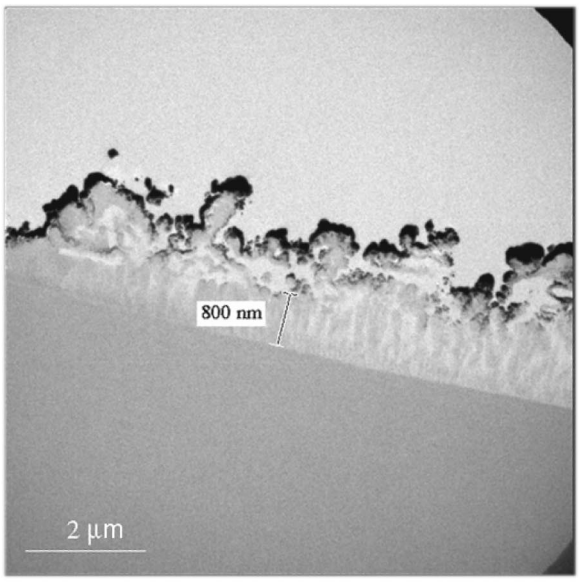


(b)

FIG. 3. TEM micrographs of the transverse section of the line structure obtained with 800 pulses at 80 mJ/cm$^2$, showing the edge of the crater (at the far left of the micrograph). (a) Overall view of the profile of the deposited material. The width of the region is 36 $\mu$m. (b) The section near the edge of the crater, showing the details of the deposited material.

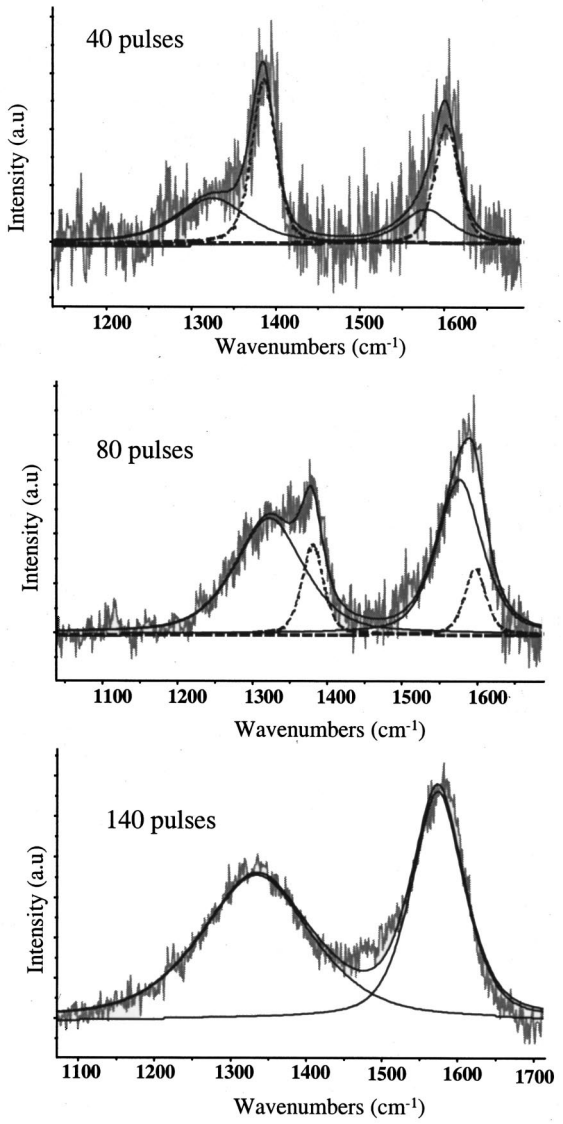


FIG. 4. Base line corrected and fitted spectra of the dark ring surrounding the craters created by 40 (top), 80 (middle), and 140 (bottom) pulses at 320 mJ/cm$^2$. Dotted line: Polyimide bands, continuous line: carbon bands.

### B. Raman-microscopy characterization of the area surrounding the ablation crater

The base line corrected Raman spectra of the rings surrounding ablation craters created with various numbers of pulses at 320 mJ/cm$^2$ are shown in Fig. 4. The spectra were measured close to the edge of the ablation crater ($\sim 5$ $\mu$m). The spectrum of the sample irradiated with 140 pulses reveals two broad overlapping peaks at 1340 [full width at half maximum (FWHM)$=156$ cm$^{-1}$] and 1580 cm$^{-1}$ (FWHM $=74$ cm$^{-1}$) and no second-order features. These signals are assigned to polycrystalline graphitic carbon with a relatively high bond angle disorder.[29,30] It is customary to refer to them as the carbon *D* and *G* bands, respectively. For low pulse numbers (40–80 pulses) the carbon *D* and *G* bands and the strongest peaks of polyimide are detectable. The PI bands can be assigned to the C=C stretching vibration of the 1,4-disubstituted phenyl ring at 1608 cm$^{-1}$ and the C–N stretching vibration of the imide system at 1395 cm$^{-1}$.[31] The four

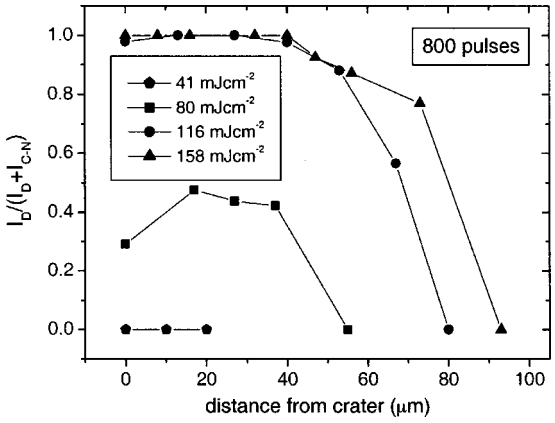


FIG. 5. Dependence of the $(I_D)/(I_D+I_{C-N})$ ratio on the distance from the crater edge. Craters were obtained with 800 pulses at various fluences.

overlapping peaks were fitted with four Gaussian–Lorentzian curves (Gaussian to Lorentzian ratio$=0.5$). The polyimide bands were fitted according to the micro-Raman spectrum of untreated polyimide: the bandwidth (FWHM 30 cm$^{-1}$) and the relative intensity ($I_{1608}/I_{1395}=0.72$) were kept constant during the fitting. The parameters of the carbon bands were allowed to vary freely. The resulting carbon *D* band was found to be centered between 1330 and 1350 cm$^{-1}$, while the *G* band was between 1580 and 1585 cm$^{-1}$. The FWHM were in the range between 100 and 180 cm$^{-1}$ for the carbon *D* band and between 50 and 80 cm$^{-1}$ for the carbon *G* band. The relative integrated intensities of the C–N stretching band of polyimide ($I_{C-N}$) and of the carbon *D* band ($I_D$) were used as probe for the thickness of the deposited carbon layer.

In Figs. 5 and 6 the $(I_D)/(I_D+I_{C-N})$ ratios are shown as a function of the distance from the edge of the ablation craters, the number of pulses and the fluence. A comparison of Fig. 5 with Table I reveals that the optically determined width of the black ring is in good agreement with the values indicated by the radial profiles of the Raman spectra. Figure 5 shows that the thickness of the carbon deposit surrounding the craters is increasing with laser fluence. For fluences close to the ablation threshold of polyimide ($\sim 40$ mJ/cm$^2$) no car-

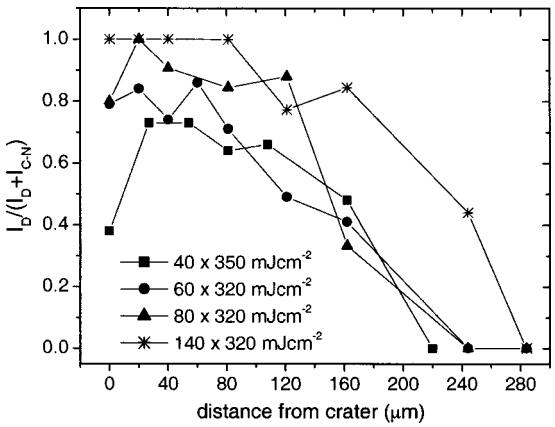


FIG. 6. Dependence of the $(I_D)/(I_D+I_{C-N})$ ratio on the distance from the crater edge. Craters were obtained with various number of pulses at 320 mJ/cm$^2$.

bon can be detected. For fluences higher than 116 mJ/cm$^2$, the ablation craters are surrounded by a circular region ($\sim$40 $\mu$m wide) where the carbon deposit masks the polyimide bands completely.

The optical microscopy images [evaluated visually from the relatively sharp transition between carbon and polyimide substrates, Fig. 2(a)] suggest no dependence of the carbon ring size on the number of laser pulses used in the ablation experiments (Table I, right column). On the contrary, the Raman radial profiles in Fig. 6 indicate that the width of the carbon ring around the craters increases slightly with the pulse number. This difference is most probably due to the different sensitivity of the two methods. The detection limit of carbon is lower for Raman spectroscopy as compared to optical microscopy.

The spatial homogeneity of the carbon deposit was evaluated by measuring the Raman spectra in three different radial directions. The analysis of the crater ablated with 80 pulses at 320 mJ/cm$^2$ suggests that the deposition is quite homogeneous at a distance of less than $\sim$50 $\mu$m from the crater edge. For instance, the $(I_D)/(I_D+I_{C-N})$ ratio at 20 $\mu$m from the crater edge in different directions varies only by 0.07. The deposit homogeneity decreases slightly at larger distances.

### C. Raman-microscopy characterization of the cone shaped structures inside the ablation craters

In Fig. 7 the SEM pictures of the cones obtained with 800 pulses at 160 mJ/cm$^2$ are shown. At the top of each cone the polymer is covered by some material ($\sim$5 $\mu$m wide) which appears white in the SEM pictures (Fig. 7, top). A larger magnification (Fig. 7, bottom) reveals that the material consists of spherical particles of $\sim$60–140 nm diameter. To determine whether the area in which this material is present has a different average chemical composition than the surrounding polymer, EDX measurements were performed at various positions. The EDX measurements reveal that calcium is a major constituent of the area covered by ''white'' material, whereas at any other position calcium is not detectable. A comparison of the EDX results obtained for the conical structures inside the craters, ablated with 800 pulses at 80 and 160 mJ/cm$^2$ and with 200 pulses at 80 mJ/cm$^2$, shows a pronounced decrease of calcium with increasing ablation fluence and pulse number.

A typical Raman spectrum of a particle with high SEM brightness on top of a conical structure is shown in Fig. 8. The carbon *G* band is at a higher frequency (1590 cm$^{-1}$) as compared to the corresponding band of the carbon deposit surrounding the ablation crater. This and the presence of a well-defined second-order peak at 2720 cm$^{-1}$ indicate that the carbon detected on top of the conical structures has a higher degree of crystallinity and lower bond angle disorder than the material deposited outside the crater.[27,32]

The intensity of the Raman carbon bands is not equal for all cone structures within a certain ablation crater. This might be due to an inhomogeneous carbon distribution within the ablation craters or to morphological features of the observed area that affect the collection of the Raman spectra. Therefore at least four conical structures within each crater were studied and the mean value $I_C$ of the sum of the intensities of the carbon *D* and *G* bands was calculated. Figure 9 illustrates how the mean intensity of the carbon bands varies with the laser fluence. It is significant that in all but one case

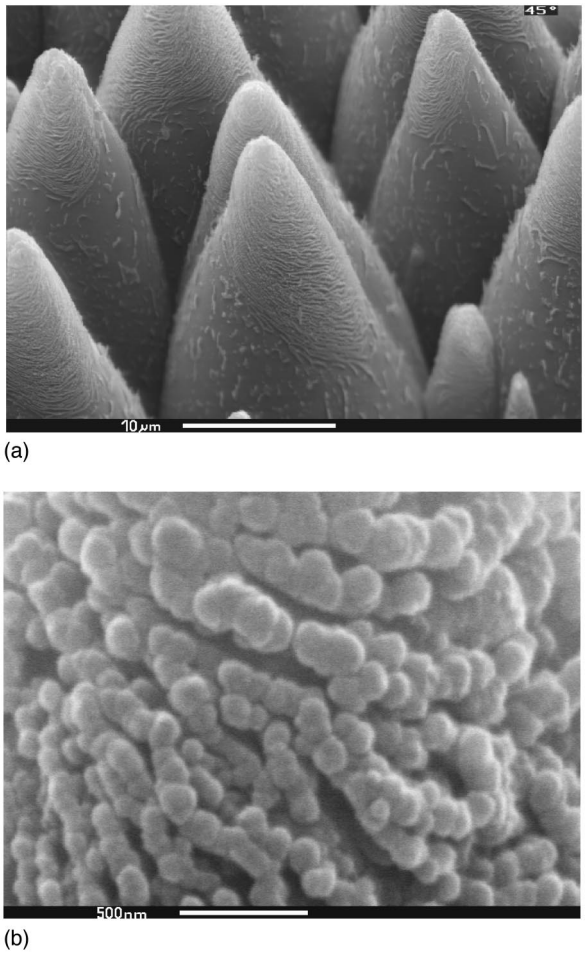


FIG. 7. SEM pictures of the area inside the crater ablated with 800 pulses at 160 mJ/cm$^2$.

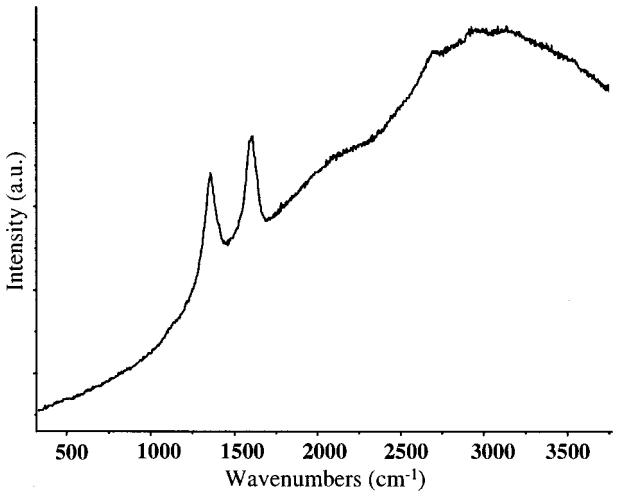


FIG. 8. Raman spectrum measured at the top of a conical structure within the crater ablated with 800 pulses at 160 mJ/cm$^2$ (the 600 grooves/mm grating was used).

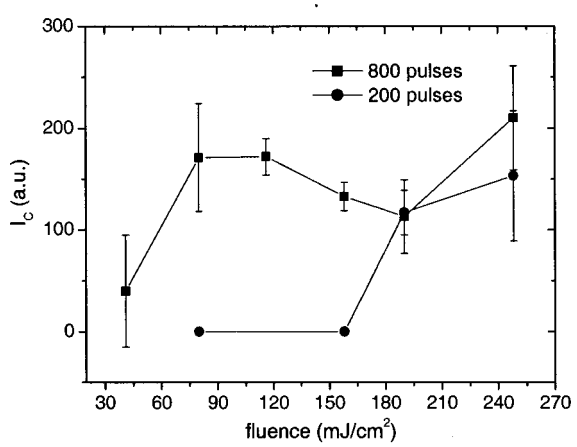


FIG. 9. Mean intensity of the carbon bands detected at the top of the conical structures. Craters were ablated with 200 and 800 pulses at various fluences. The error bars indicate the standard deviation of the measurements from different cone structures within the same ablation crater.

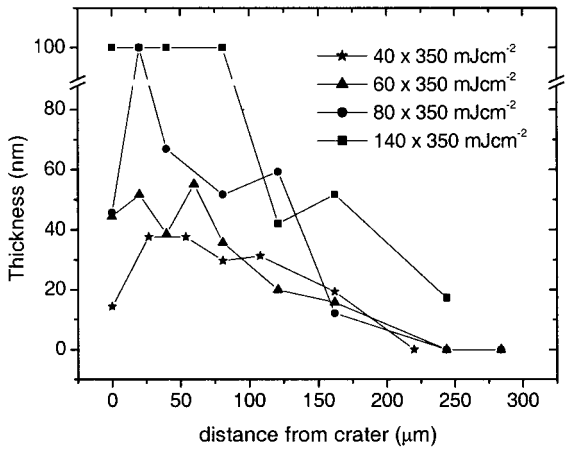


FIG. 10. Thickness of the carbon layer calculated from Eq. (6) vs the distance from the craters ablated with various pulse numbers at 320 mJ/cm$^2$.

the intensity of the carbon bands measured on top of the cone structures within the craters ablated with 200 pulses is lower than for the craters obtained by 800 pulses. In all cases no elemental carbon was detected at the crater bottom between the conical structures, but the Raman spectrum of pure polyimide was obtained.

## IV. DISCUSSION

### A. Raman-microscope characterization of the area surrounding the ablation crater

In order to estimate the thickness of the carbon deposit surrounding the ablation crater from the Raman spectra, a simple model is developed, consisting of a homogeneous layer of carbon, of thickness $a$ ($\mu$m), covering the polymer film.

If scattering phenomena due to the presence of grains, and reflections at interfaces, are neglected, the decrease of radiation intensity inside a homogeneous material $I_{IN}(t)$ can be expressed by

$$I_{IN}(t)=I_0 e^{-\varepsilon t}, \tag{1}$$

where $\varepsilon$ is the absorption coefficient of the material at the relevant wavelength, $I_0$ the intensity of the radiation before entering the material, and $t$ the penetration depth of the radiation. The intensity $I$ of a certain Raman band is then given by

$$I=\tau\int_0^\infty I_{IN}(t)se^{-\varepsilon t}dt, \tag{2}$$

where $\tau$ is a constant that includes the sensitivity of the detector and all other instrumental factors at the Raman band wavelength and $s$ is the Raman scattering factor for the specific Raman band. Inserting Eq. (1) in Eq. (2) and integrating for a two layer model, Eqs. (3) and (4) are obtained

$$I_C=\tau\int_0^a I_0 s_C e^{-2\varepsilon_C t}dt=\tau\frac{I_0 s_C}{2\varepsilon_C}(1-e^{-2\varepsilon_C a}), \tag{3}$$

$$I_{PI}=\tau\int_0^\infty I_0 s_{PI} e^{-2[a\varepsilon_C+\varepsilon_{PI}(t-a)]}dt=\tau\frac{I_0 s_{PI}}{2\varepsilon_{PI}}e^{-2a\varepsilon_C}, \tag{4}$$

where the subscripts C and PI indicate quantities relative to the carbon $D$ band and the polyimide C–N stretching band, respectively. Dividing Eq. (3) by Eq. (4)

$$\frac{I_C}{I_{PI}}=\frac{s_C}{s_{PI}}\frac{\varepsilon_{PI}}{\varepsilon_C}(e^{2\varepsilon_C a}-1) \tag{5}$$

is obtained, from which $a$ can be retrieved

$$a=\frac{1}{2\varepsilon_C}\ln\left(\frac{I_C}{I_{PI}}\frac{s_{PI}}{s_C}\frac{\varepsilon_C}{\varepsilon_{PI}}+1\right). \tag{6}$$

To estimate $[(S_{PI}/S_C)/(\varepsilon_C/\varepsilon_{PI})]$, the Raman spectra of an untreated polyimide film (thickness $\sim$125 $\mu$m) and of the thick carbon deposit surrounding a crater ablated with 250 pulses at 320 mJ cm$^{-2}$ were measured. The carbon deposit was thick enough that no Raman bands assigned to polyimide could be detected. For both samples an expression analogous to Eq. (3) in the limit of infinite thickness can be used. Thus

$$\left(\frac{I_{PI}}{I_C}\right)_{ref}=\frac{s_{PI}}{s_C}\frac{\varepsilon_C}{\varepsilon_{PI}} \tag{7}$$

is obtained. A value of $1.2\pm0.2$ was obtained experimentally for $((I_{PI})/(I_C))_{ref}$. From spectroscopic ellipsometry data on glassy carbon type $K$, a value of $\varepsilon_C$ equal to $19.3\pm0.1$ $\mu$m$^{-1}$ has been calculated.[33] The absorption coefficient of glassy carbon was used to approximate the absorption coefficient of the carbon deposit. The Raman spectra of these two materials are more or less identical, but different morphologies, e.g., density, are probable.

Figure 10 shows the thickness of the carbon layer calculated from Eq. (6) as a function of the distance from the ablation craters ablated using a fluence of 320 mJ/cm$^2$. Raman data on single, nonoverlapping craters were used in the calculation. The maximum thickness of the carbon layer that can be determined using Eq. (6) with a reasonable accuracy is $\sim$100 nm. For thicker layers only a very small C–N stretching peak of polyimide is detected, resulting in large

uncertainties in the calculation. The deposited carbon layer is thinner than 70 nm, if less than 80 pulses are used, but exceeds the upper detection limit if more pulses are used.

Comparing the calculated thickness of the carbon layer surrounding the TEM sample to the values obtained from the TEM analysis reveals that the calculation underestimates the carbon layer thickness roughly by a factor of 15. The calculated thickness of the carbon layer surrounding the line of craters used for TEM analysis is $\approx$60 nm at a distance of 25 $\mu$m from the crater edge, while the TEM analysis shows a thickness of $\approx 900 \pm 200$ nm at the same distance. The deposited material consists of two distinct layers: a more homogeneous and denser layer in direct contact with the polymer and a second layer consisting of very poorly bound material [Fig. 2(b)]. At 5 $\mu$m from the edge of the crater the thickness of each layer is 750 nm.

Including multiple reflections between the interfaces would further decrease the calculated thickness. It is most likely that the observed difference between the calculated and observed values is due to the lower absorption coefficient of the carbon deposit as compared to the applied value of glassy carbon. This is most probably due to a lower density of the deposited carbon, because the Raman spectra suggest that the chemical structure of the two materials is identical. A lower density for a material obtained from gas phase deposition (gravity induced) is expected, as supported by the inhomogeneous density observed in the TEM picture [Fig. 2(b)]. A value of $\varepsilon_C$ equal to 1.3 $\mu m^{-1}$ is obtained from Eq. (6) by using the measured (TEM) thickness of the carbon layer and the Raman intensities obtained at the same locations.

### B. Raman-microscopy characterization of the cone shaped structures inside the ablation craters

According to the model proposed by Taylor *et al.*,[28] the formation of the conical structures occurs by shading of the laser radiation by debris mainly consisting of elemental carbon deposited during the ablation process.[28] However, the variation of the intensity of the carbon Raman bands on top of the conical structures with the ablation parameters suggests a different mechanism. For the mechanism of Taylor *et al.*[28] carbon should be detected on top of the conical structures as soon as they are formed. Figure 9 shows that 200 laser pulses at 158 mJ/cm$^2$ are not sufficient to produce a detectable amount of elemental carbon on top of the conical structures, which are already visible inside the crater. Elemental carbon is only detectable after 800 pulses at this fluence, which suggests that the deposition of elemental carbon occurs after the formation of the conical structures and is not causing it.

EDX experiments reveal that a calcium containing compound is present on top of the conical structures. The fact that no other elements but carbon and oxygen are detected in amounts comparable to Ca, implies that a salt such as $CaCO_3$,$CaC_2$, or an organic Ca compound (e.g., Ca-fatty acids are in some cases used for friction control during the production of polymer films) is present. The visual appearance of the top of the conical structures did not change after a treatment in $H_2O$ or aqueous $HNO_3$($\sim$1 M) for 1 h, suggesting that no soluble materials are present.

The experimental data can be interpreted as follows. A calcium containing impurity is evenly distributed in the polymer film. The threshold fluence for this compound is higher than for polyimide, which is the case for most inorganic compounds. During irradiation the impurity particles are not ablated while the surrounding polyimide is removed. The remaining calcium containing particles shade the underlying material from the laser radiation, creating the observed conical structures. At higher laser fluences the calcium containing material is also ablated, which explains the lower density of conical structures at high fluences and the existence of a fluence window where the conical structures can be observed.

The conical structures act as nucleation centers for the growth of ordered carbon. Carbon has also a higher ablation threshold than polyimide, which results in the accumulation of carbon in a certain fluence range. While it is well known that thermal treatment increases the order of carbonaceous materials, temperatures higher than 1500 °C are in general required to promote thermal graphitization.[34] It is possible that the temperature on top of the conical structures, where no ablation takes place, is higher than in the rest of the irradiated area. Temperatures higher than 1000 °C are not very likely (decomposition temperature of PI=600 °C), even if surface temperatures between 800[6] and 1800 °C[7] were calculated from pure thermal models. Therefore, different mechanisms for the graphitization of amorphous carbon during ablation should also be considered.

Metals (e.g., Ni) are known to cause graphitization of various carbon-containing precursors at quite low temperatures (500 °C), likely to be reached during UV-laser ablation experiments.[35] Metals and metal carbides catalyze the formation of carbon nanotubes from small carbon containing molecules ($CO$, $CH_4$, $C_2H_4$) at 600 °C.[36] Therefore, it is possible that the Ca containing material may act as nucleation center for the growth of ordered carbon from the gaseous ablation products in a similar way as metal and metal carbide particles responsible for the formation of carbon nanotubes. The morphology and Raman spectra of the carbon deposit on top of the conical structures (Fig. 7, bottom) are comparable to the carbon nanohorns observed recently by Iijima *et al.*,[37] and not to carbon nanotubes. However, the carbon nanohorns were obtained during the $CO_2$ laser ablation of carbon at RT without metal catalysis. Since we observe the carbon material only on top of the Ca containing cones a mechanism presenting similarities with both the nanotube and nanohorn mechanisms might be the most probable. It is noteworthy that the experimental conditions between our experiments (RT, XeCl excimer laser, polyimide target), the formation of carbon nanohorns (RT, $CO_2$ laser, graphite target, vacuum with controlled Ar flow) and the formation of nanotubes (RT to 1200 °C, $CO_2$ or Nd:yttrium–aluminum–garnet laser, graphite target with 0.6% of metal, vacuum with controlled Ar flow) are quite different, complicating the correlation of the data.

## V. CONCLUSIONS

After irradiation of polyimide with fluences between 40 and 250 $\mathrm{mJ\,cm^{-2}}$ cone-like structures are observed in the irradiated area. On top of these cones Ca-containing species are detected which probably cause their development due to the higher ablation threshold of inorganic materials compared to polyimide. The Ca impurities shade the underlying polymer and hence give rise to the development of the cones. On top of the cones carbon with a high degree of crystallinity is detected. Carbon also exhibits a higher ablation threshold than the polymer and remains therefore on top of the cones. The increased crystallinity is probably due to a tempering like process on top of the Ca compound which is heated upon laser irradiation, or to a growth mechanism similar to those suggested for the formation of carbon nanotubes on metal particles or carbon nanohorns without metal catalysis. Ring-like structures are formed outside the ablation crater. The width of these rings increases with fluence and only slightly with the pulse number. The rings consist mainly of polycrystalline carbon with a relatively high bond angle disorder and thickness decreasing radially from the crater edge. The thickness of the deposited carbon was determined from TEM analysis. The thickness decreases nearly linearly from the crater edge ($\approx 1.6 \pm 0.3\,\mu\mathrm{m}$). The intensity ratio of Raman bands assigned to carbon and polyimide was also used to calculate the thickness of the carbon layer. The thickness calculated from the Raman bands strongly depends on the absorption coefficient, $\varepsilon_C$, of the carbon layer. Using the value of $\varepsilon_C$ measured for glassy carbon type *K* the maximum thickness that could be determined in this way was around 100 nm. This value was reached close to the crater edge for irradiation with 140 pulses at 320 $\mathrm{mJ\,cm^{-2}}$. For thicker layers the very low intensity of the bands assigned to polyimide gives rise to a large uncertainty on the calculated values. The higher thickness obtained by TEM analysis indicates that the actual absorption coefficient of the deposited carbon is about 15 times lower than the value measured for glassy carbon type *K*. This is most probably due to the lower density of the deposited material as compared to glassy carbon. Using the thickness obtained by the TEM measurements an absorption coefficient of 1.3 $\mu\mathrm{m}^{-1}$ for the deposited carbon material could be calculated from the Raman spectra.

## ACKNOWLEDGMENTS

The authors would like to thank Mrs. J. Fakan (Electron Microscopy Center, University of Lausanne) for the microtome cutting and Dr. B. Schnyder (Paul Scherrer Institut) for the spectroscopic ellipsometry measurements and fruitful discussion. This work was financially supported by the Swiss National Science Foundation.

[1] W. Kern, Semicond. Int. **8:7**, 228 (1985).
[2] H. Ahne, H. Eggers, W. Gross, N. Kokkotakis, and R. Rubner, Proceedings of the SPE Second International Conference On Polyimides, Ellenvilee, NY, Oct. 1985, p. 561.
[3] F. Bachman, Chemtronics **4**, 149 (1989).
[4] J. R. Lankard and G. Wolbold, Appl. Phys. A: Solids Surf. **54**, 355 (1992).
[5] H. Brannon, J. R. Lankard, A. I. Baise, F. Burns, and J. Kaufman, J. Appl. Phys. **58**, 2036 (1985).
[6] S. Küper, J. Brannon, and K. Brannon, Appl. Phys. A: Solids Surf. **56**, 43 (1993).
[7] N. Arnold and N. Bityurin, Appl. Phys. A: Mater. Sci. Process. **68**, 615 (1999).
[8] R. Srinivasan, R. R. Hall, W. D. Wilson, W. D. Loehle, and D. C. Allbee, J. Appl. Phys. **78**, 4881 (1995).
[9] D. L. Singleton, G. Paraskevopoulos, and R. S. Irwin, J. Appl. Phys. **66**, 3324 (1989).
[10] G. Ulmer, B. Hasselberger, H.-G. Busman, and E. E. B. Campbell, Appl. Surf. Sci. **46**, 272 (1990).
[11] J. Koren and J. T. C. Yeh, J. Appl. Phys. **56**, 2120 (1984).
[12] R. Srinivasan, B. Braren, and R. Dreyfus, J. Appl. Phys. **61**, 372 (1987).
[13] T. Lippert, E. Ortelli, J.-C. Panitz, F. Raimondi, J. Wambach, J. Wei, and A. Wokaun, Appl. Phys. A: Mater. Sci. Process. **69**, S651 (1999).
[14] T. Feurer, R. Sauerbrey, M. Smayling, and B. J. Story, Appl. Phys. A: Solids Surf. **56**, 275 (1993).
[15] Z. Ball and R. Sauerbrey, Appl. Phys. Lett. **65**, 391 (1994).
[16] T. Lippert, F. Zimmermann, and A. Wokaun, Appl. Spectrosc. **47**, 1931 (1993).
[17] P. E. Dyer, S. D. Jenkins, and J. Sidhu, Appl. Phys. Lett. **49**, 453 (1986).
[18] B. Hopp, Z. Bor, E. Homolya, and E. Mihalik, Proc. SPIE **3423**, 389 (1998).
[19] J. E. Andrew, P. E. Dyer, D. Foster, and P. H. Key, Appl. Phys. Lett. **43**, 717 (1983).
[20] T. Bahners and E. Schollmeyer, J. Appl. Phys. **66**, 1884 (1989).
[21] K. Tonyali, L. C. Jensen, and J. T. Dickinson, J. Vac. Sci. Technol. A **6**, 941 (1988).
[22] P. E. Dyer and R. J. Farley, Appl. Phys. Lett. **57**, 765 (1990).
[23] E. Arenholz, M. Wagner, J. Heitz, and D. Bäuerle, Appl. Phys. A: Solids Surf. **55**, 119 (1992).
[24] S. Hajatdoost and J. Yarwood, Appl. Spectrosc. **50**, 558 (1996).
[25] S. Hajadoost, M. Olsthoorn, and J. Yarwood, Appl. Spectrosc. **51**, 1784 (1997).
[26] A. Cuesta, P. Dhamelincourt, J. Laureyns, A. Martinez Alonso, and J. M. D. Tascon, Appl. Spectrosc. **52**, 356 (1998).
[27] A. Cuesta, P. Dhamelincourt, J. Laureyns, A. Martinez-Alonso, and J. M. D. Tascon, Appl. Spectrosc. **52**, 356 (1998).
[28] R. S. Taylor, K. E. Leopold, D. L. Singleton, G. Paraskevopoulos, and R. S. Irwin, J. Appl. Phys. **64**, 2815 (1988).
[29] F. Tuinstra and J. L. Koenig, J. Chem. Phys. **53**, 1126 (1970).
[30] R. O. Dillon, J. A. Woollam, and V. Katkanat, Phys. Rev. B **29**, 3482 (1984).
[31] H. Ishida, S. T. Wellinghof, E. Baer, and J. L. Koenig, Macromolecules **13**, 826 (1980).
[32] J. M. Stencel, *Raman Spectroscopy for Catalysis* (Van Nostrand Reinhold, New York, 1990), Chap. 4, p. 128.
[33] H. G. Tompkins and W. A. McGrahan, *Spectrocopic Ellipsometry and Reflectometry, A User's Guide* (Wiley, New York, 1999), pp. 19–20.
[34] M. Nakamizo, R. Kammereck, and P. L. Walker, Jr., Carbon **12**, 259 (1974).
[35] M. Yudasaka, K. Tasaka, R. Kikuchi, Y. Ohki, S. Yoshimura, and E. Ota, J. Appl. Phys. **81**, 7623 (1997).
[36] C. Laurent, E. Flahaut, A. Peigney, and A. Rousset, New J. Chem. **22**, 1229 (1998).
[37] S. Iijima, M. Yudasaka, R. Yamada, S. Bandow, K. Suenaga, F. Kokai, and K. Takahashi, Chem. Phys. Lett. **309**, 165 (1999).